Finite-Element Simulation of Mixing: 1. Two-Dimensional Flow in Periodic Geometry

Th. Avalosse
POLYFLOW s.a., 16 Place de l'Université, B-1348 Louvain-la-Neuve, Belgium

M. J. Crochet
CESAME, Université Catholique de Louvain, 4 avenue G. Lemaître, B-1348 Louvain-la-Neuve, Belgium

Complex mixing flows and mixing parameters are calculated to evaluate mixing quality on the basis of kinematic parameters together with a statistical analysis. The results allow for a comparative evaluation in terms of geometry and flow parameters. The evaluation is limited to two-dimensional flows with moving boundaries in periodic motion such as the flow in the cross section of a twin-cam mixer. The finite-element calculation requires a remeshing procedure for every time step with special techniques to upgrade mixing variables from one time step to the next. The relative mixing quality of single cam and co- or counterrotating cam devices are compared by evaluating segregation scale, length stretch, and efficiency. The numerical results exhibit a good correspondence with their experimental counterpart.

Introduction

Present analysis of mixing devices is essentially limited to two-dimensional flows, with the possible addition of an axial flow, because of the computational cost. Simplifications are introduced to reduce actual three-dimensional flows to their 2-D counterparts. Typically, Wang and White (1989) and Kim and White (1990) use averages across the thickness of the channel to calculate the flow in a twin-screw extruder. For a Banbury mixer, Cheng and Manas-Zloczower (1989, 1990) neglect transverse material flow to reduce the analysis to two dimensions. Progress in 3-D flow analysis now leads to the analysis of more realistic configurations. Yang and Manas-Zloczower (1992) studied the flow in a Banbury mixer for a set of cam configurations, while Tanguy et al. (1992) calculate the flow in a helical mixer.

Early evaluation of the quality of a mixing device or protocol was based on the homogenization of the fluid (see, e.g., Tadmor and Gogos, 1979). Statistical measurements were based on the evolution of the concentration of a minor component in the mixture with respect to its major counterpart (Schofield, 1976; Fan et al., 1970). The segregation scale, typical of these calculations (Dankwertz, 1951) is representative of the average size of the zones occupied by the minor component and thus of the texture of the mixture. It should be pointed out that the segregation scale is relative in the sense that it depends upon the initial configuration of the mixture; as such, it is less helpful in comparing two different processes.

It is now recognized that, in laminar flow, the amount of deformation is the major indicator of the quality of the mixing process. A general theory developed by Ottino (Ottino et al., 1981; Ottino, 1989) is based on the calculation of several kinematic variables, representative of the generation of interface, along pathlines of material particles in the flow. Another important parameter associated with the calculation of pathlines in open domains is the distribution of residence times (Danckwerts, 1953). The quantification of mixing with the help of kinematic parameters has been developed by Ottino, initially on the basis of analytical flow solutions (see, e.g., Khakhar et al., 1987), while more recent articles (e.g., Jana et al., 1994) rely entirely on computational techniques. In addition to the study of transported quantities, additional tools such as manifold structure and Melnikov technique are now used for the analysis (Jana and Ottino, 1992). In a recent article, Souvaliotis et al. (1995) point out the increasing importance of numerical simulation in the analysis of mixing. While recognizing the interest of computational techniques, they observe that numerical errors may jeopardize the accuracy of the results.

In this article, we limit ourselves to 2-D flows with boundaries in periodic motion. A typical application is the flow in

the cross section of a twin-cam mixer where cams are either co- or counterrotating. The simulation is difficult from a numerical viewpoint because the calculation is performed on a complex domain of constantly varying shape; the finite-element calculation requires a remeshing procedure for every time step. Moreover, special techniques are needed to upgrade the mixing variables from one time step to the next. The procedure allows us to quantify the relative mixing quality of single-cam and co- or counterrotating-cam devices. In a second article, we analyze 3-D flows in open domains. Our purpose is to develop numerical methods for evaluating mixing quality on the basis of kinematic parameters together with a statistical analysis.

In the following section, we recall the basic equations and define the kinematic and mixing variables that we want to measure. Special attention is given in the third section to the calculation of mixing variables on the basis of finite-element results. The fourth and fifth sections are devoted to the analysis of single and twin triangular cams. In the fourth section, we compare the finite-element results with experimental data on the flow of glucose in a twin-cam device. In the fifth section, we use the mixing variables to evaluate the relative merits of single- and twin-cam systems.

Basic Equations and Mixing Variables

We analyze plane mixing flows in domains with time-periodic boundary conditions. The flow is confined between a fixed external boundary and two rotating cams which can be co- or counterrotating. At time $t = 0$, a curve C^0 separates fluid A from fluid B; we wish to predict the motion of interface $C(t)$ and to quantify the mixing of A and B.

The flow calculation rests on strong hypotheses:

i. Fluids A and B have the same rheological behavior; the flow calculation is identical to that of a single homogeneous fluid;
ii. Chemical reactions and diffusion do not occur between fluids A and B; interfacial tension vanishes;
iii. Inertia and body forces are not taken into account;
iv. There is no void formation in the flow;
v. The fluids do not slip along fixed or moving walls.

Let Ω^0 and Ω denote the domains occupied by the fluid at times 0 and t, respectively. Let $\boldsymbol{X}$ denote the position of a material point P in Ω^0 and $\boldsymbol{x}$ the position in Ω; $\boldsymbol{F}$ the deformation gradient; and $\boldsymbol{C} = \boldsymbol{F}^T\boldsymbol{F}$, the right Cauchy–Green strain tensor. The velocity gradient and the rate of deformation tensor at time t are denoted by $\boldsymbol{L}$ and $\boldsymbol{D}$, respectively.

Consider in Ω^0 a material fiber $\boldsymbol{dX}$ with a unit orientation $\boldsymbol{M}$ that deforms into a material fiber $\boldsymbol{dx}$ with a unit orientation $\boldsymbol{m}$ at time t. Ottino (1989) shows that the length stretch λ is given by

$$\lambda(\boldsymbol{X}, \boldsymbol{M}, t) = |d_x| / |dX| = (\boldsymbol{M}\cdot\boldsymbol{CM})^{1/2}, \tag{1}$$

where a dot denotes the scalar product, while the new orientation $\boldsymbol{m}$ is given by

$$\boldsymbol{m} = \frac{\boldsymbol{FM}}{\lambda}. \tag{2}$$

A good mixing quality is usually associated with high values of λ throughout time and space. A local evaluation of the efficiency of mixing (Ottino et al., 1981) is given by the ratio

$$e_\lambda(\boldsymbol{X}, \boldsymbol{M}, t) = \frac{\dot{\lambda}/\lambda}{D} = \frac{\boldsymbol{m}\cdot\boldsymbol{Dm}}{D}, \tag{3}$$

where $D = (trD^2)^{1/2}$. We note that e_λ is a local measurement along the path of a material point; and $< e_\lambda >$ denotes the time-averaged efficiency for the same material point between times 0 and t.

Let $c(\boldsymbol{X}, t)$ denote the concentration of fluid A throughout the mixing process. Since no diffusion occurs between fluids A and B, c equals either 0 or 1 and remains constant along the trajectory of a material point. The concept of concentration allows us to introduce the notion of segregation scale (Dankwertz, 1951; Tadmor and Gogos, 1979). At time t, consider a set of J pairs of material points separated by a distance r: for the jth pair, let c_j' and c_j'' denote the concentrations at both points of the pair; moreover, let $\bar{c}$ denote the average concentration of all points and σ_c the standard deviation. At time t, the correlation coefficient $R(r,t)$ for the concentration is defined as follows:

$$R(r,t) = \frac{\sum_{j=1}^{J} (c_j' - \bar{c})(c_j'' - \bar{c})}{J\sigma_c^2}. \tag{4}$$

The correlation coefficient is positive for low values of r and changes sign at $r = \xi$. The segregation scale $S(t)$ is defined as

$$S(t) = \int_0^\xi R(r,t)\, dr; \tag{5}$$

it measures the size of the regions of homogeneous concentration.

While quantities such as λ, e_λ, and $\langle e_\lambda \rangle$ are proper to the flow, irrespective of the initial concentration, the segregation scale $S(t)$ is affected by the flow but depends strongly on the initial distribution of concentration.

Evaluation of Mixing Variables

We use the finite-element method although, for the present class of problems, it might be more appropriate to use boundary elements. The reason is that our essential objective is to solve 3-D problems where the use of boundary elements may not be optimal.

A finite-element mesh is generated for every discrete time t_i; let us examine in Figure 1 a typical mesh generation at time t_i. The angular position of the triangular cams is specified at the outset. The domain surrounded by the outer boundary of the flow is covered with a finite-element mesh. The location of the cams allows us to draw a line that crosses the elements of the preassigned mesh. It is then found that some elements are crossed by the inner boundary, while most of them may be used as such for calculating the flow. The line of segments separating such elements from those crossed by the inner boundary is called the generating line. The gen-

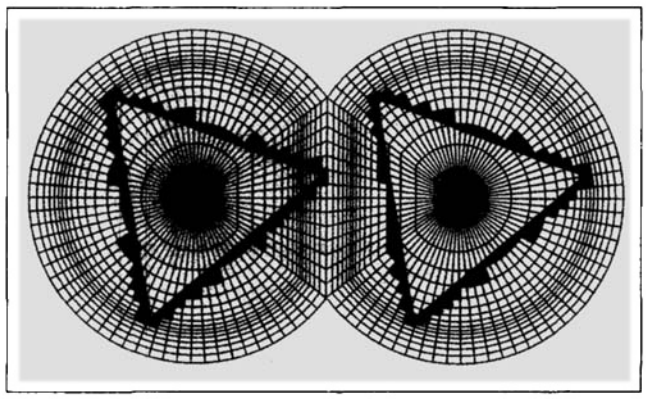

Figure 1. Original mesh, generating line, and generating zone for automatic mesh generation during the rotation of the cams.

erating zone is located between the generating line and the inner boundary. An automatic mesh generator based on the Delaunay triangulation (Watson, 1981) is then used to define an appropriate finite-element mesh in the generating zone that is compatible with the filled elements of the preassigned mesh. An advantage of the present procedure is that, from one discrete time to the next, most elements remain unchanged and only a moderate amount of elements are affected by the cam's rotation. The procedure was developed by Couniot (1991) and used for the numerical simulation of injection molding (see, e.g., Crochet et al., 1994).

Since inertia terms are not taken into account in our analysis, the calculation reduces to a series of Stokes flows at every discrete time. We use the classic velocity–pressure formulation with $P^2 - C^0$ elements for the velocity field and $P^1 - C^0$ elements for the pressure. Thus, at every discrete time t_i, we dispose of a finite-element mesh compatible with the location of the cams and a set of nodal values for the velocity vector.

Kinematic variables

Let us assume that the location $\boldsymbol{x}(t)$ of a material point is known at time t together with its velocity field $\boldsymbol{v}(t)$. We wish to calculate the location $\boldsymbol{x}(t+\Delta t)$ by solving the equation

$$\frac{\boldsymbol{x}(t+\Delta t)-\boldsymbol{x}(t)}{\Delta t}=\theta \boldsymbol{v}(t+\Delta t)+(1-\theta)\boldsymbol{v}(t). \qquad (6)$$

When $\theta = 0$, 0.5, or 1, Eq. 6 corresponds, respectively, to Euler explicit, Crank–Nicolson, or Euler implicit method; it is solved by means of Newton's method with a predictor–corrector algorithm (Avalosse, 1994).

We also evaluate the deformation gradient $\boldsymbol{F}(t+\Delta t)$ with respect to the configuration at time $t = 0$, that is, we solve the equation,

$$\frac{\boldsymbol{F}(t+\Delta t)-\boldsymbol{F}(t)}{\Delta t}=\theta \boldsymbol{L}(t+\Delta t)\boldsymbol{F}(t+\Delta t)+(1-\theta)\boldsymbol{L}(t)\boldsymbol{F}(t), \qquad (7)$$

which constitutes a linear system of equations in $\boldsymbol{F}(t+\Delta t)$. Once $\boldsymbol{F}(t+\Delta t)$ and $\boldsymbol{L}(t+\Delta t)$ are known at the new location of the material point, we calculate the remaining kinematic variables such as $\boldsymbol{C}$, λ, $\boldsymbol{m}$, and e_λ.

Let us assign to N material points an initial orientation $\boldsymbol{M}$ that does not need to be identical for all points. While tracking the material points as a function of time, we calculate successive values of $\boldsymbol{F}$, $\boldsymbol{C}$, $\boldsymbol{m}$, and thus λ, e_λ, and $\langle e_\lambda \rangle$. A finite-element representation of λ, e_λ, and $\langle e_\lambda \rangle$ considered as fields over the flow domain is unfeasible. Such a representation would imply an interpolation between points located at a distance of the order of the element size h, which is generally large with respect to the striation thickness in a mixing process. A global representation of λ, e_λ, and $\langle e_\lambda \rangle$ is better obtained by associating a material point with a small square of side dl; the color of the square is itself associated with the value of the field to be represented. The quality of the representation increases with the number of points N.

When the number of material points is sufficiently large, we may proceed with a statistical treatment of the calculated quantities. In particular, let us consider the distribution function F_α associated with the field α. The quantity $F_\alpha(\beta,t)$ is defined as follows:

$$F_\alpha(\beta,t)=P[\alpha(t)\le\beta], \qquad (8)$$

where the right-hand side is the probability that the variable α will be smaller than β at time t.

A new graph of the distribution function is calculated at every time t. An easier representation of the mixing process is based on the time dependence of percentiles. For the field α, let us define $\alpha_p(t)$ such that

$$F_\alpha(\alpha_p,t)=p, \qquad (9)$$

where $\alpha_p(t)$ indicates that, at time t, p % of the material points have a value of α lower than $\alpha_p(t)$. Several examples are shown in the fifth section. We note in particular that, for the length stretch λ, it is recommended that $\log_{10}\lambda$ be used instead of λ in view of the fairly large values attained by the stretch in the mixing process.

Concentration

Our next concern is to calculate the time-dependent concentration throughout the flow domain. A first straightforward approach is to assume a finite-element representation for the concentration c and to integrate the transport equation $\dot{c}=0$. It is soon discovered, however, that the pattern of the concentration field in the mixing process has a characteristic length that is much smaller than the element size h. As a consequence, the finite-element representation of the concentration is fraught with spatial oscillations and with discretization errors (see also Löhner et al., 1984).

A second approach is to calculate the motion of the material line $C(t)$ separating fluids A and B. One considers a set of material points $C(t)$ that are connected by straight segments. Whenever the distance between two points exceeds some critical length, new material points are added. Such a technique has its limitations, such as the loss of geometrical details through the straight-line interpolation between material points. Above all, the necessary number of material points on $C(t)$ increases so fast that the calculation becomes quickly

prohibitive (Franjione and Ottino, 1987). The calculation of the material line $C(t)$ is used in the fourth section.

A third method consists of subdividing the flow domain at time $t = 0$ into a set of small square cells of size dl: a uniform grid of $N_x \times N_y$ cells is overlaid on the flow domain. Each square is associated with a specific color or concentration. When time progresses, we calculate the new location of the center of each cell, which is again surrounded by a small square with the initial color of the cell. Quite clearly, for a given number of cells, the computation time remains the same at every time step; moreover, once the successive coordinates of material points are stored, a minor effort is needed to calculate at time t the concentration corresponding to another set of initial conditions. The limitation of the method lies in the size of the material point identified by the cell, but the number of points can be increased at will.

Segregation scale

Let us now assume that we have tracked N material points and that, among these points, we select at random P pairs of material points. Let d_{max} be the maximum distance between two material points in the flow domain, and let us consider K intervals of equal length between 0 and d_{max}. Let us examine J pairs of points such that their relative distance lies between $(k-1)d_{max}/K$ and kd_{max}/K, where $1 \le k \le K$. For each pair j, $1 \le j \le J$, we calculate the relative distance d_j between the points and the correlation

$$R_j = \frac{(c_j' - \bar{c})(c_j'' - \bar{c})}{\sigma_c^2}, \tag{10}$$

where $\bar{c}$ is the average concentration, σ_c the standard deviation, and c_j', c_j'' are the concentrations of the material points constituting the pair. At time t, we obtain the value R_k of the correlation coefficient corresponding to the distance r_k with the definition

$$r_k = \frac{1}{J} \sum_{j=1}^{J} d_j, \tag{11a}$$

$$R_k = \frac{1}{J} \sum_{j=1}^{J} R_j. \tag{11b}$$

The correlation coefficient $R(r,t)$ is completed by a linear interpolation through the discrete values defined by Eq. 11. The segregation scale $S(t)$ may then be easily calculated by numerical integration on the basis of Eq. 5.

Accuracy

The accuracy of the numerical method has been investigated in detail by Avalosse (1994).

First, we have verified convergence of the algorithm on the basis of the Couette flow, for which an analytical solution is available. Three meshes used for the convergence study are shown in Figure 2. The meshes contain 96, 384 and 1,536 elements, respectively. The inner radius is 0.5, the outer radius 1. The angular velocity vanishes on the inner circle and is equal to 1 rad/s on the outer circle. We have selected the

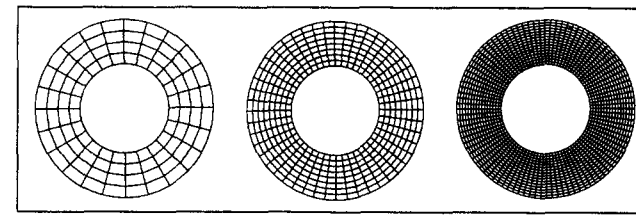

Figure 2. Three meshes used for testing convergence in Couette flow.

trajectory of a material particle initially at mid-distance between both circles. One reason for our choice is that such a particle is located at the interface between finite elements and would be adversely affected by discretization errors.

First we verified that the Crank–Nicolson scheme is superior to the Euler implicit and explicit methods for our problem. In particular, it can be shown that phase errors are much larger with Euler's methods.

For a fixed value of the time step ($2\pi/100$ s), we then tested the distance between the analytical coordinates of the material point and their calculated counterpart as a function of the angle of rotation. After 20π s (ten rotations), such an error reached the value of 0.003 times the outer radius for the three meshes. We have performed the same analysis on the intermediate mesh, for three different time steps: $2\pi/10$ s, $2\pi/100$ s, and $2\pi/1{,}000$ s. The maximum error, after 20π s, due to the angular locations of the particle (and not its radius) is, respectively, 0.3, 0.003 and 0.00003, depending upon the time step. The error on the deformation gradient follows the same trend. After 20π s, the relative error on the deformation gradient reaches, respectively, 25%, 0.25%, and 0.075% for the three time steps. The relative error is defined as follows:

$$\epsilon(t) = \frac{\max | \boldsymbol{F}_{num} - \boldsymbol{F}_{an} |}{\max | \boldsymbol{F}_{an} |}, \tag{12}$$

where $\boldsymbol{F}_{num}$ and $\boldsymbol{F}_{an}$ correspond to the components of the deformation gradient tensors at time t. With the intermediate time step, we obtain an acceptable level of accuracy. This time step corresponds to an angular rotation of 3.6° of the outer circle.

As a further test, before dealing with the triangular cams, we considered a problem that does not require remeshing in order to evaluate the phase error. The device and the finite-element mesh are shown in Figure 3. The circular cams are corotating counterclockwise with an angular velocity of 0.5 rpm. By means of an experimental device to be explained in the fourth section, we observe and calculate the time deformations of a spot of colored fluid; the results are shown in Figure 4 up to a rotation of the cams equal to 8π. The time step is chosen such that the angular rotation between two successive steps is 4°. There is a good correspondence between experimental and numerical results, although we observe an increasing phase error as a function of time.

Finally, we studied the convergence of our statistical results as a function of the number of material points. This analysis was done on the corotating twin-cam system (studied in detail in the following section). The triangular cams are

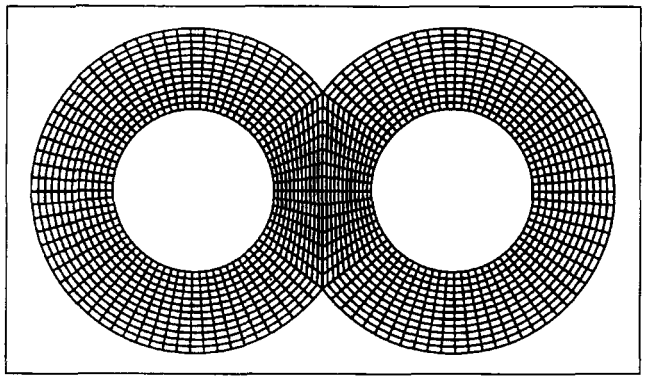

Figure 3. Finite-element mesh for a corotating cam system (1,728 elements).

rotating counterclockwise with an angular velocity of 1 rpm. A new mesh is generated for every 4° of rotation of the cams. We selected grids with 65×40, 150×85, and 335×190 cells, leading to 1,560, 7,724 and 38,170 points inside the computational domain, respectively. The statistical results are essentially the same for all three grids. In our examples below, we select the intermediate grid with 150×85 cells for the twin-cam systems (and 85×85 cells for the single-cam system), which keeps the computational time within acceptable bounds.

The initial orientation field $\boldsymbol{M}$ has little impact on the results; uniformly oriented and random fields produce essentially the same results. To calculate the correlation coefficient $R(r,t)$ and the segregation scale $S(t)$ in the examples below, we chose a value of K (Eqs. 10 and 11) such that the width of one interval corresponds to the cell side dl. Our numerical experiments showed that our results do not depend upon J in Eq. 10 provided $J \geq 200$.

Experimental Validation

In order to test the capabilities of the numerical method, we have mounted an experimental device shown in Figure 5. It has the shape of a kneading-through device with two triangular cams that can either be co- or counterrotating; the rotation of the cams is activated through the motion of a notched belt. The horizontal cavity is filled with an aqueous solution of glucose; its depth is 25 mm. The viscosity of the solution should be low enough to avoid 3-D effects due to the combined action of gravity and free surface and high enough to avoid color dispersion when a spot of colored glucose (of the same viscosity) is spread on top of the transparent one. A viscosity of 50 PaS was adopted in the experiment. The rate

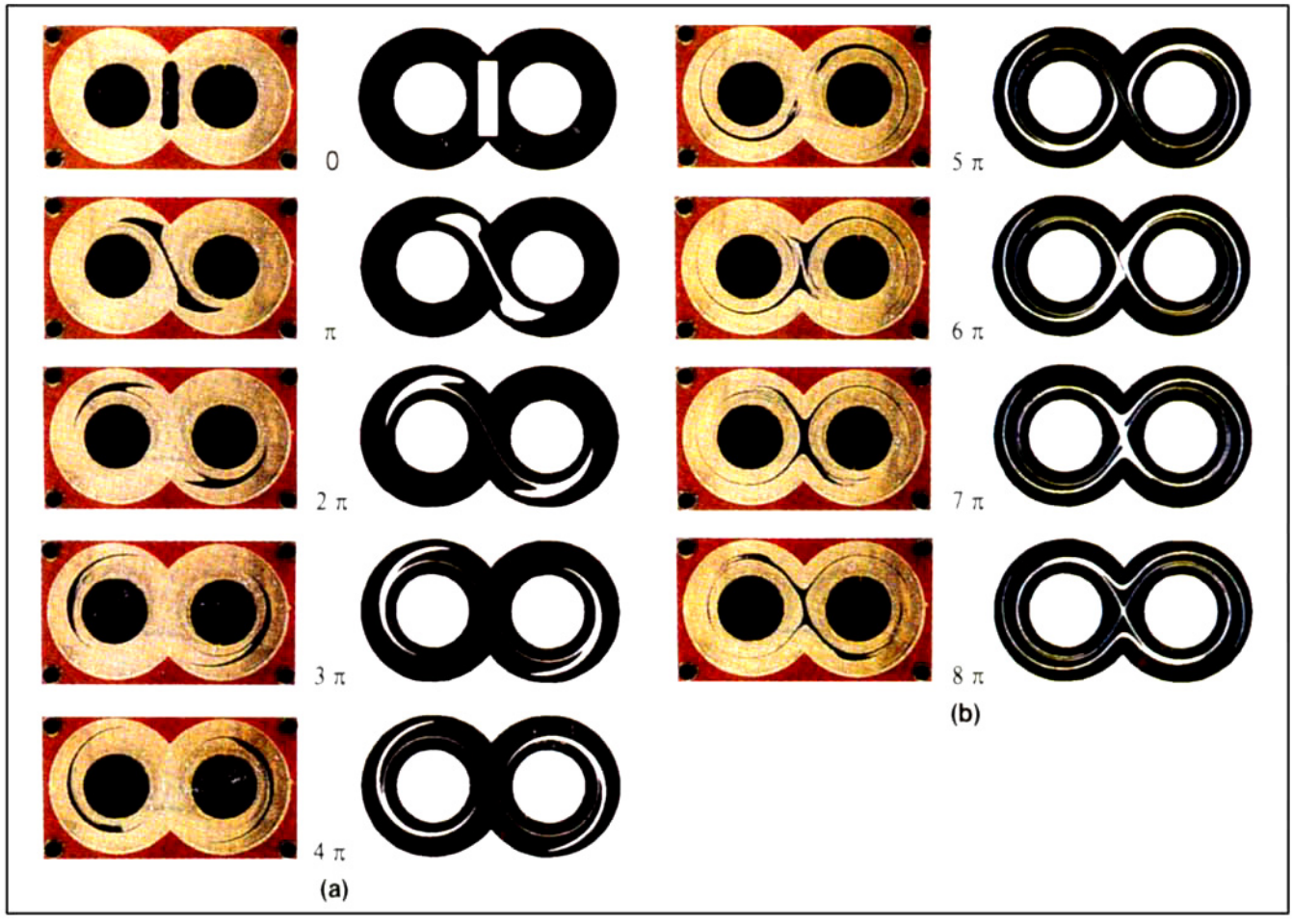

Figure 4. Dispersion of a spot in a corotating cam system: comparison between experimental and numerical results; each successive section corresponds to an additional rotation of π.

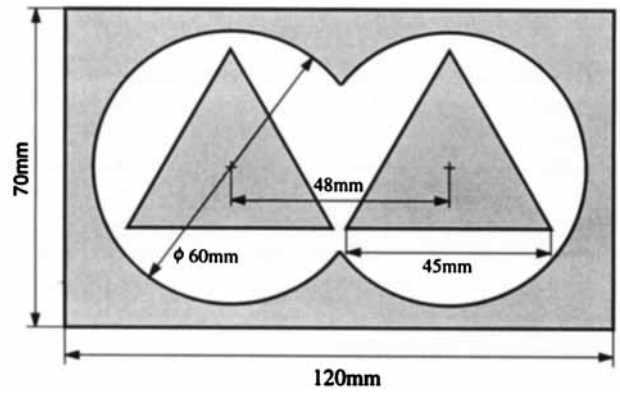

Figure 5. Dimensions (in mm) of the kneading-through device for experimental validation.

of rotation of the cams was 0.5 rpm. The Reynolds number is of the order of 10^{-3}. A photograph of the surface is taken after every rotation of $\pi/3$ of the cams.

The reference finite-element mesh is shown in Figure 6a. It is based on several convergence trials dealing with Couette flow. The central (black) spots are covered by the rotating cams. For every 4 degrees of rotation of the cams, a new mesh is generated on the basis of the reference mesh. A typical example of automatic generation that corresponds to a generic position of counterrotating cams is shown in Figure 6b. The design of the reference mesh is such that small elements are found in regions where a higher accuracy is needed, such as near the tips of the cam. At every time step, we may thus easily calculate the velocity field as shown in Figure 6c and perform the calculation of the kinematic variables associated with mixing.

In the present section, we calculate the evolution of the colored spot through the motion of the closed curve $C(t)$. Material points along $C(t)$ are such that their distance can-

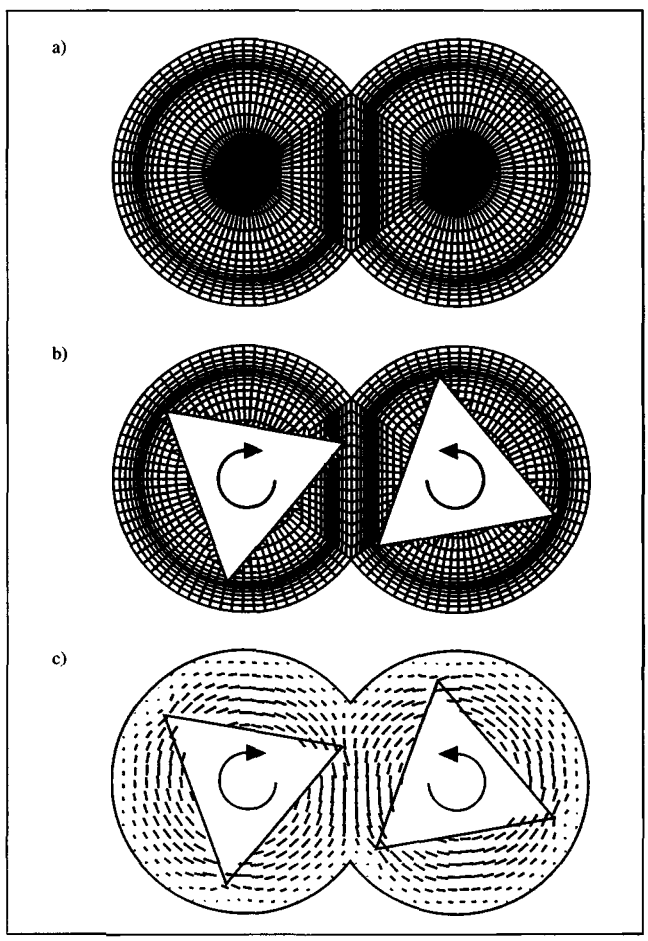

Figure 6. Reference finite-element mesh (a), the actual mesh (b), and the velocity field (c) for an arbitrary position of the cams.

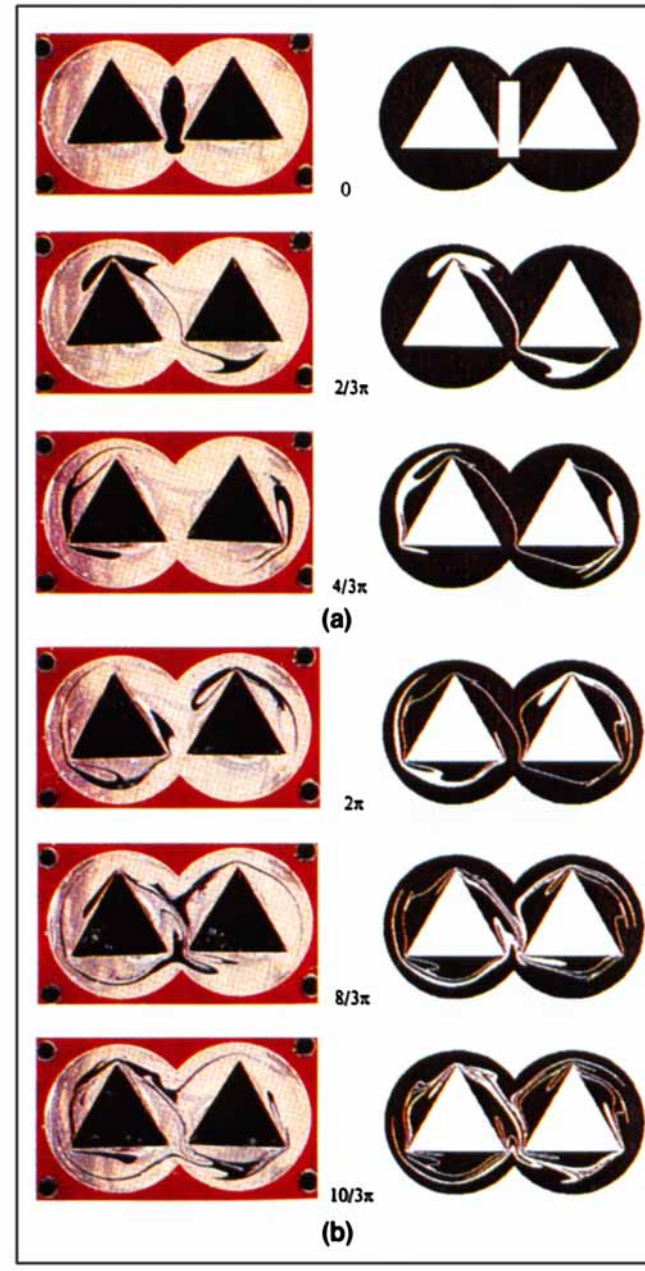

Figure 7. Comparison on the dispersion of a spot between experimental and numerical results for corotating cams; each successive section corresponds to an additional rotation of $2\pi/3$.

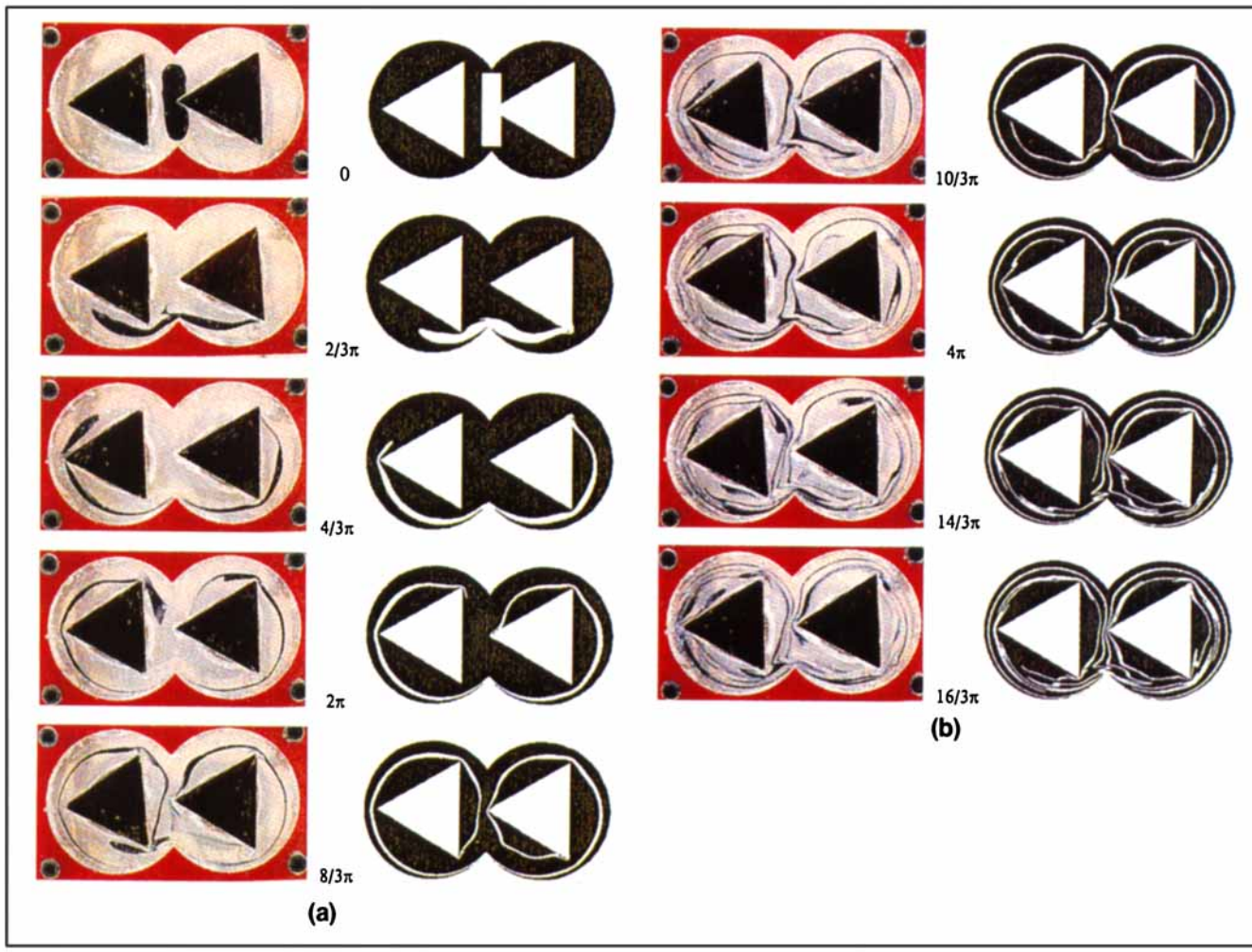

Figure 8. Comparison on the dispersion of a spot between experimental and numerical results for counterrotating cams; each successive section corresponds to an additional rotation of $2\pi/3$.

not exceed 0.2 mm (the side of the cams is 45 mm long). Additional material points are added in the course of time in order to satisfy that rule. The initial shape of the spot in numerical calculations is a rectangle that is 8 mm wide and 31 mm high.

Figure 7 compares experimental and numerical results for the case of counterclockwise corrotating cams. We note that the initial spot is rectangular on the numerical simulation but deviates slightly from that shape in the experiment (which was carried out after the simulations). Experimental and numerical results are compared after every rotation of $2/3\pi$ of the cams. These results show a good qualitative agreement between experiments and simulation.

A good agreement is also found in the case of counterrotating cams shown in Figure 8. The cam on the left rotates clockwise, the one on the right counterclockwise. In this case, we find that the colored spot is first squashed at the bottom and then stretched in the opposite direction. After three rotations, the colored fluid is stretched throughout the flow domain. A simple inspection of the bottom half of Figure 7 and the last four sections of Figure 8 reveals that the corotating system is a better mixer than the counterrotating one. This visual impression is quantified in the next section.

Our calculations show the ability of the numerical simulation to reproduce details of the flow. One can, however, observe differences between experiments and simulation. In the last half of Figure 7, beyond a 2π rotation, the global pattern is the same, but it seems that some material particles do not show the same angular positions on both sides of the figure. In particular, Figure 8 shows that the colored material near the left lobe moves faster in the experiment than in the simulation. Observed differences between experiments and simulations are due to the following several factors:

- The calculation is based on a finite-element discretization of the flow domain and of the velocity field; time is also discretized in order to calculate pathlines and kinematic variables; numerical errors may accumulate and affect the patterns shown in Figures 7 and 8.
- The experimental spot differs from the previously adopted rectangular shape in the simulation.
- The drying of glucose at the free surface locally increases the viscosity.
- Possible 3-D effects are neglected in the 2-D simulation; quite notably, the bottom surface is a no-slip boundary that induces shear stress.

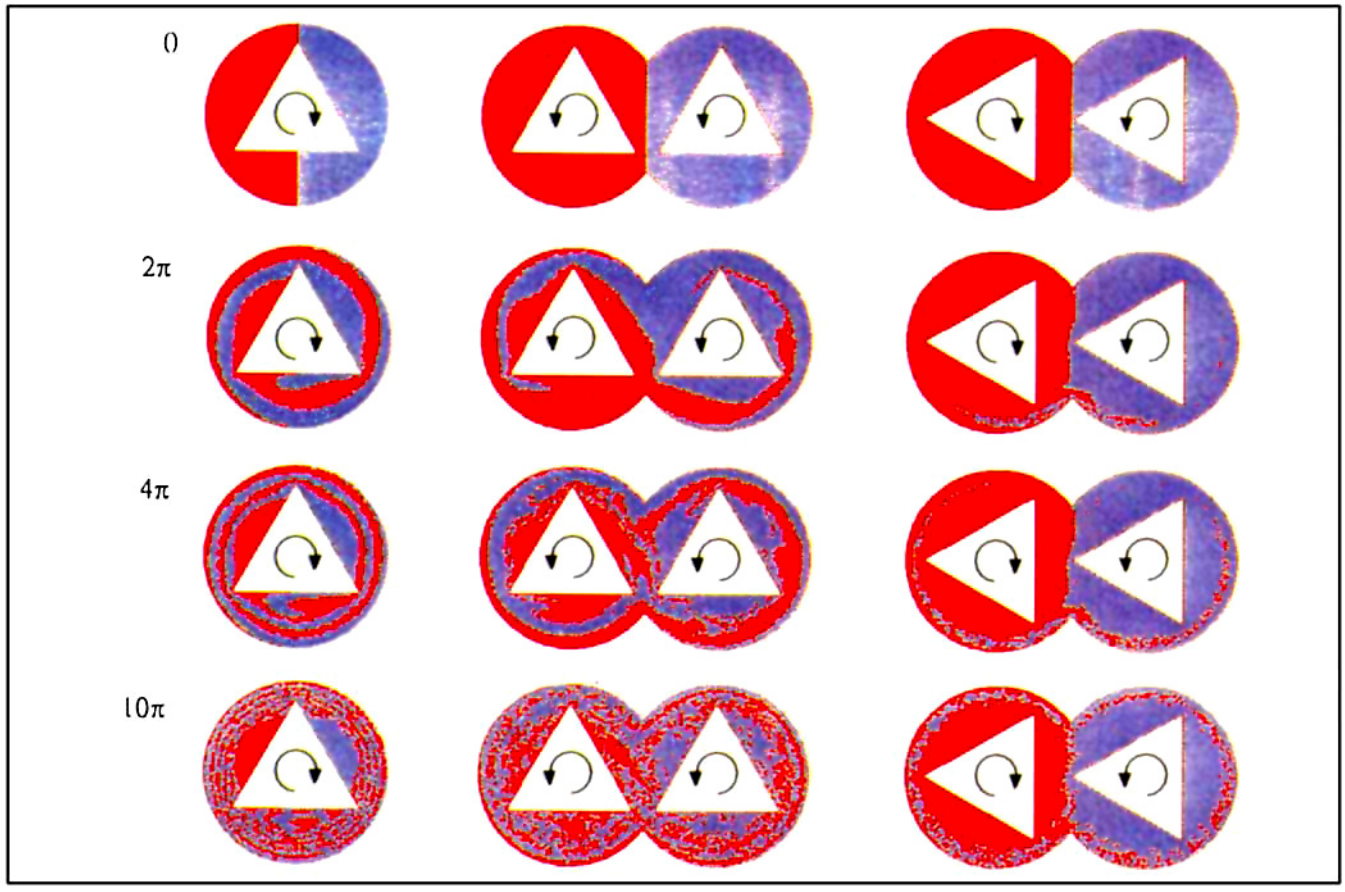

Figure 9. Evolution of the concentration for the single-cam, corotating twin-cam, and counterrotating twin-cam systems corresponding to 0, 1, 2 and 5 rotations of the cams.

- A flow singularity at the tips of the cams (Moffatt, 1964) leads to a local inaccuracy in calculating the trajectories.
- The discretization of the spot affects its shape; some deformations increasing with time are lost forever in the simulation (Souvaliotis et al., 1995).
- Very thin areas of the spot may not be visible on the photographs, while the printer draws lines of constant thickness.

Numerical Evaluation

Let us now use the numerical and statistical tools to evaluate the quality of mixing. In addition to the co- and counterrotating devices of the preceding section, we include a single-cam device: its outer radius is 60 mm, as in Figure 5, while the triangular cam has the same dimensions as before. For the single-cam device, the flow calculation is easier since the velocity field is obtained by rotating the outer boundary (without remeshing) instead of the cam (with remeshing). We now compare the three systems: single cam (SC), corrotating twin cams (TC+), and counterrotating twin cams (TC−).

Let us first calculate the time-dependent concentration. It is assumed that half the system is filled with red fluid while the other half is blue. A grid of 150×85 cells covers the TC systems, while 85×85 cells are used for SCs. Figure 9 shows the evolution of the concentration after 2π, 4π, and 10π rotations of the cams. With SC, we observe that every turn of the cam creates a new striation. However, since the tips of the cam lie on the same circle, there is very little mixing. With TC+, there is a significant mass transfer between the lobes. The mixing near the cams after 10π is better than with SC, but one can still identify regions of uniform color. With TC−, there is very little mixing by comparison with SC and TC+.

The time evolution of the segregation scale $S(t)$ is shown for the three systems in Figure 10. The difference between TC+ and TC−, with the same initial conditions, is very clear: $S(t)$ decreases slowly for TC−, while it reaches the discretization limit of the order of the cell size dl after 4π for TC+. The same is true for SC, which starts, however, from different initial conditions associated with a lower value of $S(0)$. From these curves, we cannot conclude that SC is better than the other two devices; the apparent better performance of SC is due to a different initial configuration of the concentration field.

The distribution of the length stretch is a distinctive feature of the simulation. Figure 11 shows the distribution of λ after an angle of rotation of 10π. The superiority of TC+ is evident. We find a fairly uniform distribution of λ throughout the flow domain except near the sides of the cams where we observe localized regions of low length stretch. In TC−, we find that larger regions near the boundary of the cams exhibit little stretching; the same is true with SC: the lack of

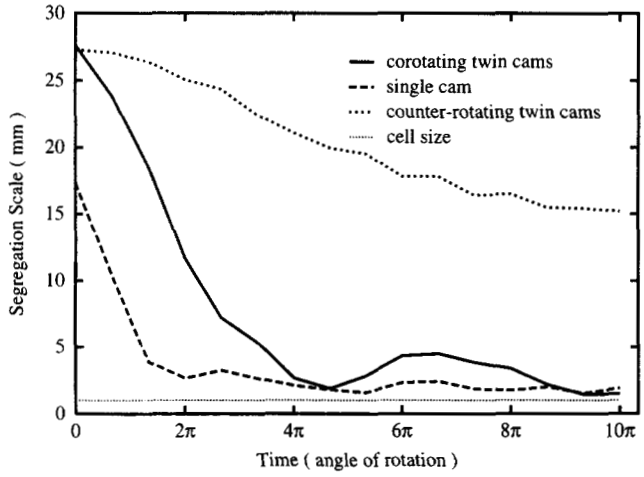

Figure 10. Time evolution of the segregation scale for the single-cam, corotating twin cam, and counterrotating twin-cam systems.

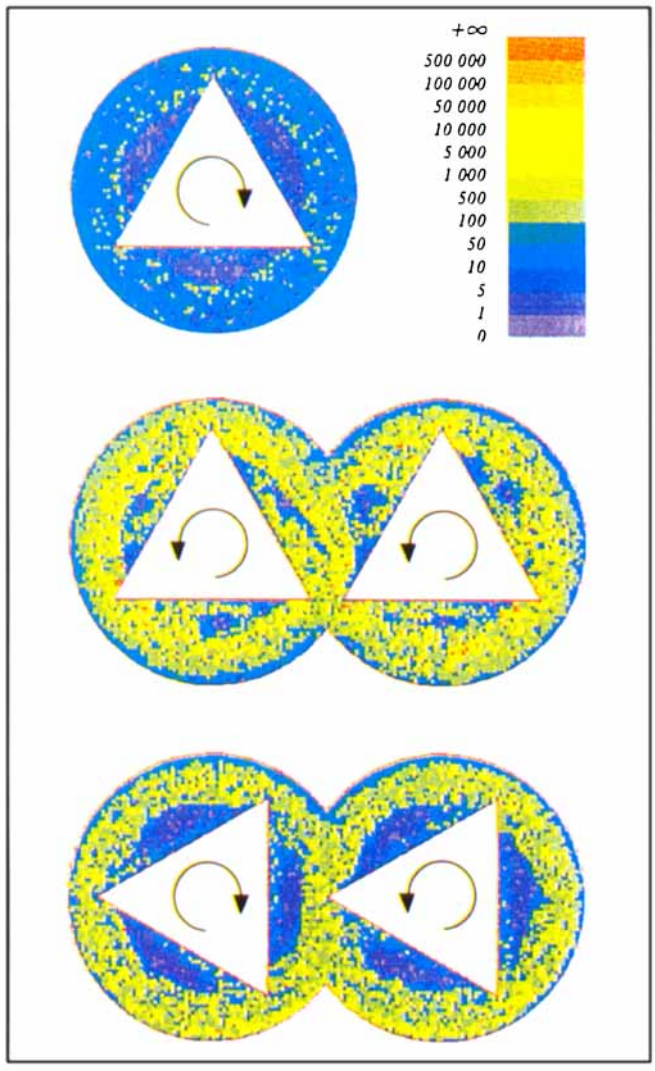

Figure 11. Distribution of the length stretch after 5 rotations of the cams for the single-cam, corotating twin-cam, and counterrotating twin-cam systems.

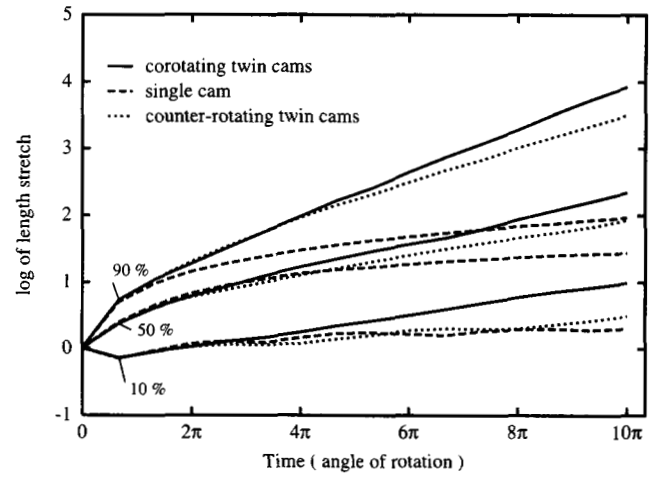

Figure 12. Percentiles of the logarithm of the length stretch as a function of time for the single-cam, corotating twin-cam, and counterrotating twin-cam systems.

exchange between the lobes together with local recirculation prevent large values of λ. These different behaviors are confirmed by the graph of percentiles shown in Figure 12. Due to very large values of the length stretch, a logarithmic scale is used for λ. The highest value of λ is always found with TC+. After five rotations of the cams, 50% of the material points have a length stretch lower than 240 with TC+, 100 with TC−, and 30 with SC.

The efficiency of mixing, e_λ, is a quantity that essentially depends on the flow and only slightly on the initial orientation. A typical example is shown in Figure 13 where we show the distribution function of the instantaneous efficiency for TC+. The initial distribution of e_λ changes from that after one turn because the orientation $\boldsymbol{m}$ differs from $\boldsymbol{M}$; however, it is little affected by additional rotations. Figure 14 shows the percentiles of instantaneous efficiency as a function of time for the three systems. We find that they indeed remain essentially constant beyond the first rotation of the cams. It is

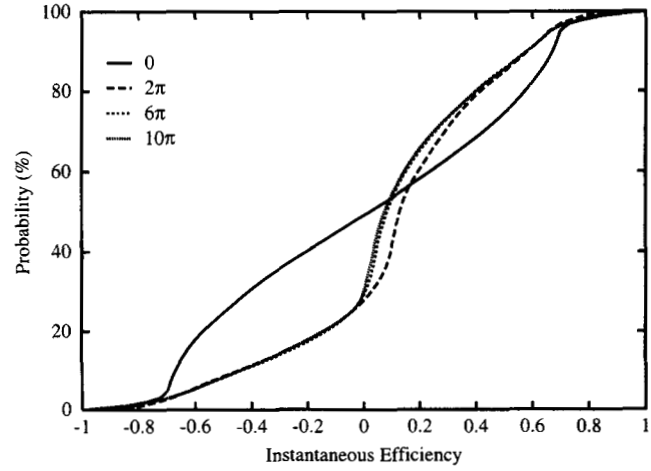

Figure 13. Distribution function of the instantaneous efficiency for the corotating twin-cam system after 0, 1, 3 and 5 rotations of the cams.

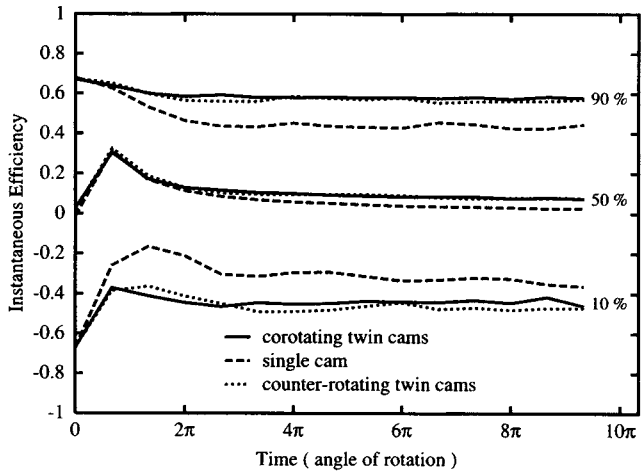

Figure 14. Percentiles of the instantaneous efficiency as a function of time for the single-cam, corotating twin-cam, and counterrotating twin-cam systems.

interesting to see that, for all three systems, 50% of the material points are associated with a local efficiency lower than 0.1.

The time-averaged efficiency is fairly low for all material particles. Figure 15 shows the percentiles of $\langle e_\lambda \rangle$ as a function of time. It is found that the three systems produce essentially the same results; we observe a decrease of the 50th and 90th percentiles of $\langle e_\lambda \rangle$ as t^{-1} because the flows are essentially dominated by shear (Ottino and Chella, 1983). However, for the TC systems, there exists a zone between the cams where reorientation occurs, leading to better stretching; this transient phenomenon has little influence on $\langle e_\lambda \rangle$, but is well measured by λ. We observe that $\langle e_\lambda \rangle$ is eventually everywhere positive, while the instantaneous efficiency e_λ may be negative.

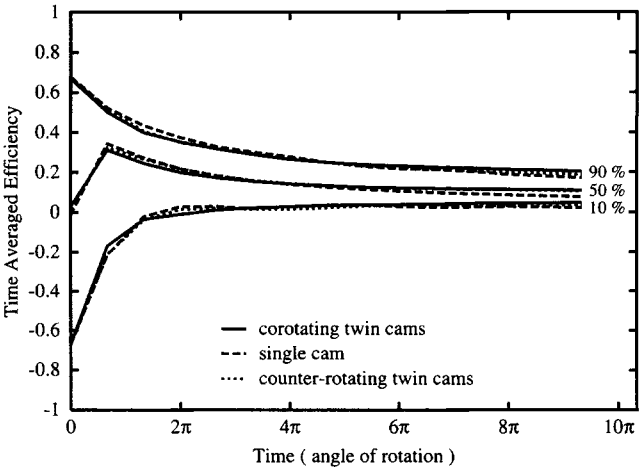

Figure 15. Percentiles of the time-averaged efficiency as a function of time for the single-cam, corotating twin-cam, and counterrotating twin-cam systems.

Conclusions

We have developed a finite-element method to calculate velocity fields and kinematic variables in 2-D flows surrounded by moving rigid boundaries. The method applies in particular to flows around rotating cams of arbitrary shape. Several accuracy tests have allowed us to select the numerical features of the flow of a Newtonian viscous fluid around co- and counterrotating triangular cams; they include the finite-element mesh, the time step, and the density of the material particles for the evaluation of mixing quality. Additionally, we have compared numerical results to experimental observations. The comparison is good, although phase errors increase with the number of rotations. We have also developed statistical tools that, on the basis of kinematic variables, allow us to perform an objective evaluation of mixing and to compare protocols.

A finite-element visualization of parameters such as the length stretch λ and the concentration c is unavailable because the characteristic length of their distribution is generally much smaller than the element size. A good visual evaluation of mixing is obtained through a colored plot of the values of λ (or rather log λ) and c attached to a set of material particles. This qualitative evaluation is effectively quantified by a plot of percentiles as a function of the number of rotations, which we consider as the most useful tool in our developments. The efficiency, e_λ, and its time average are less discriminating. We have also calculated the segregation scale; its use is limited by the fact that it strongly depends on the initial conditions of the concentration.

Acknowledgments

Th. Avalosse gratefully acknowledges the support of Solvay s.a. The work of M. J. Crochet was performed under the aegis of Interuniversity Attraction Poles initiated by the Belgian State, Prime Minister's Office.

Literature Cited

Avalosse, Th., "Simulation Numérique du Mélange Laminaire par Eléments Finis," PhD Thesis, Univ. Catholique de Louvain, Louvain-la-Neuve, Belgium (1994).

Cheng, J., and I. Manas-Zloczower, "Hydrodynamic Analysis of a Banbury Mixer. 2-D Flow Simulations for the Entire Mixing Chamber," *Poly. Eng. Sci.*, **29**, 1059 (1989).

Couniot, A., "Développement d'un Algorithme de Remaillage Automatique pour la Simulation du Moulage par Injection," PhD Thesis, Univ. Catholique de Louvain, Louvain-la-Neuve, Belgium (1991).

Crochet, M. J., F. Dupret, and V. Verleye, "Ch. 11—Injection Molding," *Flow and Rheology in Polymer Composites Manufacturing*, S. G. Advani, ed., Elsevier Science, Amsterdam, p. 415 (1994).

Danckwerts, P. V., "The Definition and Measurement of Some Characteristics of Mixtures," *Appl. Sci. Res.*, *A*, **3**, 279 (1951).

Danckwerts, P. V., "Continuous Flow Systems. Distribution of Residence Times," *Chem. Eng. Sci.*, **2**, 1 (1953).

Fan, L. T., S. J. Chen, and C. A. Watson, "Solids Mixing," *Ind. Eng. Chem.*, **62**, 53 (1970).

Franjione, J. G., and J. M. Ottino, "Feasibility of Numerical Tracking of Material Lines and Surfaces in Chaotic Flows," *Phys. Fluids*, **30**, 3641 (1987).

Jana, S. C., G. Metcalfe, and J. M. Ottino, "Experimental and Computational Studies of Mixing in Complex Stokes Flows: The Vortex Mixing Flow and Multicellular Cavity Flows," *J. Fluid Mech.*, **269**, 199 (1994).

Jana, S. C., and J. M. Ottino, "Chaos-Enhanced Transport in Cellular Flows,' *Philos. Trans. R. Soc. Lond. A*, **338**, 519 (1992).

Khakhar, D. V., J. G. Franjione, and J. M. Ottino, "A Case Study of Chaotic Mixing in Deterministic Flows: the Partitioned-Pipe Mixer," *Chem. Eng. Sci.*, **42,** 2909 (1987).
Kim, M. H., and J. L. White, "A Non-Newtonian Model of Flow in Forward and Backward Pumping Screw Regions of a Modular Tangential Counter-Rotating Twin-Screw Extruder," *J. Non-Newtonian Fluid Mech.*, **37,** 37 (1990).
Löhner, R., K. Morgan, and O. C. Zienkiewicz, "The Solution of Non-Linear Hyperbolic Equation Systems by the Finite Element Method," *Int. J. Numer. Methods Fluids*, **4,** 1043 (1984).
Moffatt, H. K., "Viscous and Resistive Eddies near a Sharp Corner," *J. Fluid Mech.*, **18,** 1 (1964).
Ottino, J. M., and R. Chella, "Laminar Mixing of Polymeric Liquids; A Brief Review and Recent Theoretical Developments," *Poly. Eng. Sci.*, **23,** 357 (1983).
Ottino, J. M., W. E. Ranz, and C. W. Macosko, "A Framework for Description of Mechanical Mixing of Fluids," *AIChE J.*, **27,** 565 (1981).
Ottino, J. M., *The Kinematics of Mixing: Stretching, Chaos, and Transport*, Cambridge University Press, New York (1989).
Schofield, C., "The Definition and Assessment of Mixture Quality in Mixtures of Particulate Solids," *Powder Technol.*, **15,** 169 (1976).
Souvaliotis, A., S. C. Jana, and J. M. Ottino, "Potentialities and Limitations of Mixing Simulations," *AIChE J.*, **41,** 1605 (1995).
Tadmor, Z., and C. G. Gogos, *Principles of Polymer Processing*, Chaps. 7 and 11, Wiley, New York (1979).
Tanguy, P. A., R. Lacroix, F. Bertrand, L. Choplin, and E. Brito de la Fuente, "Finite Element Analysis of Viscous Mixing with a Helical Ribbon-Screw Impeller," *AIChE J.*, **38,** 939 (1992).
Wang, Y., and J. L. White, "Non-Newtonian Flow Modelling in the Screw Regions of an Intermeshing Corotating Twin Screw Extruder," *J. Non-Newtonian Fluid Mech.*, **32,** 19 (1989).
Watson, D. F., "Computing the N-Dimensional Delaunay Tessellation with Application to Voronoï Polytopes," *Comp. J.*, **24,** 167 (1981).
Yang, H., and I. Manas-Zloczower, "3D Flow Field Analysis of a Banbury Mixer," *Theoretical and Applied Rheology*, Vol. 1, P. Moldenaers and R. Keunings, eds., Elsevier, Amsterdam, p. 408 (1992).

Manuscript received Sept. 25, 1995, and revision received Sept. 30, 1996.